THE JOURNAL OF PHYSICAL CHEMISTRY C
A JOURNAL OF THE AMERICAN CHEMICAL SOCIETY

pubs.acs.org/JPCC Article

Interfacial Phase Modulation-Induced Structural Distortion, Band Gap Reduction, and Nonlinear Optical Activity in Tin-Incorporated Ga_2O_3

Guillermo Gutierrez, Emma M. Sundin, Paul Gaurav Nalam, Vishal Zade, Rebecca Romero, Aruna N Nair, Sreeprasad Sreenivasan, Debabrata Das, Chunqiang Li, and C. V. Ramana*

Cite This: *J. Phys. Chem. C* 2021, 125, 20468−20481 Read Online

ABSTRACT: We report the structural chemistry and optical properties of tin (Sn)-mixed gallium oxide (Ga_2O_3) compounds, where the interfacial phase modulation-induced structural distortion in turn induces variations in the band gap and nonlinear optical activity. The Sn incorporation into Ga_2O_3 causes significant reduction in the band gap and induces nonlinear optical activity upon chemical composition tuning. Detailed investigation performed on the structural chemistry, phase stabilization, surface morphology, and optical and electrochemical properties of Sn-mixed Ga_2O_3 compounds ($Ga_{2-2x}Sn_xO_3$, $0.00 \leq x \leq 0.3$, Ga-Sn-O) indicates that the Sn-incorporation-induced effects are significant. To produce Ga-Sn-O materials of high structural and chemical quality, we adopted a simple solid-state chemical reaction route involving first calcining and then sintering the material at higher temperatures. Structural chemistry analyses of sintered Ga-Sn-O compounds by X-ray diffraction (XRD) showed solid solution formation at lower Sn concentrations ($x \leq 0.10$). The XRD analyses indicate the SnO_2 secondary phase formation at higher ($x > 0.10$) Sn concentrations. Surface morphology analysis using scanning electron microscopy (SEM) also showed a positive relationship between phase separation and Sn concentration. Optical absorption spectra showed a substantial redshift in the band gap (E_g), which would allow Ga-Sn-O compounds to have wide spectral selectivity. At higher Sn concentrations ($x = 0.25$−0.30), corroborating with structural/chemical analyses, an additional lower-energy sub-band transition that explicitly corresponds to SnO_2 appears in the optical absorption data. Importantly, the evidence of nonlinear optical activity in Ga-Sn-O, which is otherwise not traditionally known for such an activity, as well as dipolar- and quadrupolar-shaped dependence of activity with the polarization angle of the excitation source was detected. At higher concentrations ($x \geq 0.15$), Sn was found to be insoluble, which can be attributed to Ga_2O_3 and SnO_2 possessing different formation enthalpies and cation (Ga^{3+} and Sn^{4+}) chemistries. The fundamental scientific understanding of the interdependence of synthetic conditions, structure, chemistry, and optical and electrochemical properties could be useful to optimize Ga-Sn-O inorganic compounds for optical, optoelectronic, and photocatalytic device applications.

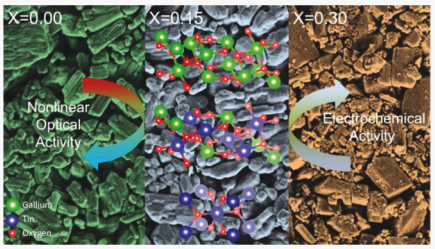

■ INTRODUCTION

Recently, gallium oxide (Ga_2O_3) has been receiving significant attention from the scientific and engineering research communities because of its diverse structural chemistry, physical and chemical properties, novel phenomena, and technological applications.[1−18] The ability for integration into numerous scientific and technological applications, which include utilization in electronics, optoelectronics, neuromorphic engineering, energy storage and conversion, catalysis, and chemical sensors, has given Ga_2O_3 and Ga_2O_3-based alloys immense recognition in the mainstream of current research topics.[1−10] The specific application potential of these materials includes, but not limited to, the design and development of deep ultraviolet (UV) photodetectors, field-effect transistors (FETs), high-power electronic devices, sensors, solar cells, transparent conducting oxides (TCOs), cost-effective light-emitting diodes (LEDs), liquid eutectic contact, and photocatalysts.[8−18]

The enormous interest in Ga_2O_3 is primarily derived from its thermodynamic stability and wide band gap.[1−7,18,19] The band gap of β-Ga_2O_3 is ∼4.8 eV, although the reported values vary in the range of 4.5−5.0 eV based on the methods employed for synthesis.[1−18] The wide band gap of β-Ga_2O_3 corresponds to the second largest after that of diamond and is considerably greater than those of other TCOs such as In_2O_3, SnO_2, and ZnO. Even after decades of research around β-Ga_2O_3, it has been only in the last decade or so that research interest has picked up momentum to utilize their extreme properties.

Received: May 5, 2021
Revised: August 6, 2021
Published: September 10, 2021

https://doi.org/10.1021/acs.jpcc.1c04005
J. Phys. Chem. C 2021, 125, 20468−20481

Substantial recent work on β-Ga_2O_3 materials in terms of device applications has hinted toward a possible replacement of the currently well-established SiC and GaN power devices, which operate at extreme or ultrahigh voltages.[16−18] On the other hand, Ga_2O_3 is also an interesting material from a fundamental science perspective; it exhibits six different polymorphs, namely, the α, β, γ, δ, ε, and κ phases. However, compared to other polymorphs, the β-Ga_2O_3 polymorph exhibits a very high and favorable chemical and thermal stability.[19] β-Ga_2O_3 crystallizes in the monoclinic crystal structure in the C2/m space group. The processing and characterization of β-Ga_2O_3 is a very fascinating research problem, especially realizing the high-quality and defect-free bulk crystals and nanostructures for device applications in electronics and optoelectronics.

There has been a substantial amount of experimental as well as theoretical investigations (involving density functional theory, DFT, calculations) on β-Ga_2O_3 and β-Ga_2O_3-based alloys and composites. Most importantly, several researchers have directed their efforts toward studying the effect of doping different ions with variable chemical valence states into β-Ga_2O_3 and toward understanding the dopant effect on the structural chemistry and electronic/electrochemical properties of resulting materials. For instance, the control over electrical conductivity with Si doping into Ga_2O_3 proves to be effective because Si^{4+} acts as an electron donor and increases the free carrier concentration by a few orders of magnitude as compared to the undoped Ga_2O_3.[20−22] Si doping proved to be quite useful in tailoring the electrical conductivity and in enhancing the *n*-type conductivity.[20−22] Similarly, the recent DFT calculations provide deeper insights into the chemical formation energy and the defect nature of transition-metal dopants into β-Ga_2O_3.[23−25] Using the DFT calculations, the shallow donor nature with a low formation energy was established for the Nb dopant as opposed to the deep donor behaviors of W, Mo, and Re as dopants into β-Ga_2O_3.[23] The photocatalytic activity of doped β-Ga_2O_3 indicates that the specific ion and associated chemistry can influence the performance greatly.[26−30] For instance, studies focused on the photocatalytic activity using zinc (Zn^{2+}) for doping reported that the photocatalytic performance was significantly improved because of the associated charge separation arising at the heterojunction of $ZnGa_2O_4$:β-Ga_2O_3.[26] However, studies performed on lead (Pb^{2+}) doping showed a decline in the photocatalytic activity.[26] The observed decline in the photocatalytic activity was attributed to the generation of recombination centers arising because of Pb^{2+} doping into β-Ga_2O_3.[26,27] In this context, Zadeh and co-workers demonstrated that the sub-band energy-state-assisted efficient photocatalysis using Ga_2O_3 nanoparticles assimilated into the liquid metal/metal oxide configuration.[28,29]

A wealth of information is also available in the literature with respect to the optical and optoelectronic properties. Radovanovic et al. demonstrated that tailoring the size, shape, and phase of Ga_2O_3 and their polymorphs provides excellent opportunities to derive tunable optoelectronic properties and performance.[1,6] For instance, size- and phase-controlled colloidal γ-Ga_2O_3 nanocrystals demonstrated tunable photoluminescence (PL) from UV to blue.[1,6] Similarly, complex PL properties were obtained by Eu doping into colloidal γ-Ga_2O_3 nanocrystals that exhibit red and blue emission, resulting from intra-4f orbital transitions. Dual blue−green PL emission of Tb^{3+}-doped Ga_2O_3 nanocrystals was also demonstrated.[31] The transition-metal (TM) ion, such as Fe, Ti, and W, mixing or alloying into β-Ga_2O_3 indicated significant reduction and redshift in the optical band gap.[15,32−37] However, the amount of redshift and spectral selectivity were found to be dependent on the specific TM ion used for doping. Similarly, several existing studies suggest that the overall chemistry, electronic structure, and optical properties can be tailored by doping the metal ions into β-Ga_2O_3 thin films or nanomaterials. The Cu-doped β-Ga_2O_3 thin films prepared by sputter deposition showed a marked decrease in the optical band gap.[38] The band gap reduction was attributed to the impurity energy levels formed by Cu ions doped into β-Ga_2O_3.[38] A red-shifted band gap was observed for W- and Ti-doped β-Ga_2O_3 polycrystalline thin films produced using different thin-film deposition techniques.[32,33,39,40] Nb doping into β-Ga_2O_3 also decreases the optical band gap; thin films deposited show a reduced band gap because of unoccupied new energy levels by Nb that are below the conduction band edge.[41] Thus, it is clear that the structural, chemical, and electronic properties of the resulting materials highly depend on the nature, chemistry, valence state, and site occupation of the specific dopant ions into β-Ga_2O_3.

The present work deals with the Sn-mixed Ga_2O_3 nanocrystalline compounds' synthesis and their structural chemistry, morphology, and electronic, electrochemical, and nonlinear optical properties. The obvious reasons for the consideration of these important Sn-mixed Ga_2O_3 inorganic compounds are as follows. Similar to Ga_2O_3, SnO_2 is an interesting semiconductor and is quite important for electronic and optoelectronic applications. With a band gap energy of 3.6 eV, *n*-type semiconducting SnO_2 has been explored widely for utilization in transparent conductive electronics and integrated chemical sensors.[42−49] The ability to respond selectively to both oxidizing and reducing gases makes SnO_2 materials suitable for the design and development of novel sensors.[42,44,45] Therefore, incorporating Sn into Ga_2O_3 and understanding the fundamental aspects of the resulting compounds and their physical/chemical/electronic properties are beneficial not only from a fundamental science perspective but also to derive new properties and phenomena, which can facilitate designing materials for advanced electronics and energy-related applications.

The doping of Sn into Ga_2O_3 has been considered by several researchers in recent years.[50−59] The Sn-doped Ga_2O_3 single crystals were produced using the float zone method, where electrical resistivity and carrier concentration were shown to be tailored based on the amount of Sn doped into Ga_2O_3.[58] Similarly, the viability of Sn-doped Ga_2O_3 as a GaN-based optical device for TCOs has also been explored.[57] Zhao et al. reported that Sn doping reduces the resistivity of Ga_2O_3.[54] The Sn-doped Ga_2O_3 films produced by metal−organic chemical vapor deposition (MOCVD) indicated *n*-type conductivity with a carrier concentration of 1.95×10^{17} cm^{-3} and a Hall mobility of 0.9 cm^2 V s^{-1}.[54] Similarly, Ohira et al. reported that Sn doping improves electrical conductivity and Hall mobility while postdeposition annealing further improves the electrical properties.[50] β-Ga_2O_3 single crystals doped with different Sn^{4+} concentrations produced using the floating zone technique were transparent and conductive; their optical properties and electrical conductivities were strongly influenced by the Sn^{4+} concentrations and annealing.[58] Most recently, Ryou et al. studied the structural, chemical, and photocatalytic properties of Sn-doped β-Ga_2O_3 nanomaterials synthesized using a facile

https://doi.org/10.1021/acs.jpcc.1c04005
J. Phys. Chem. C 2021, 125, 20468−20481

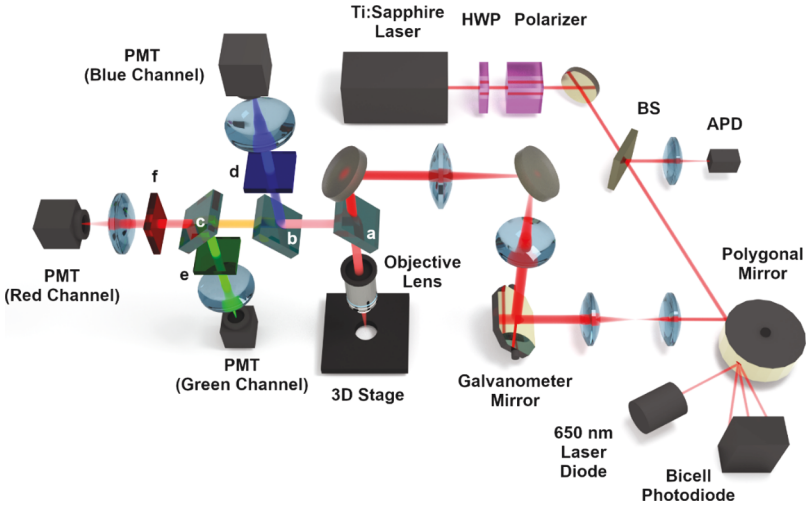

Figure 1. Laser scanning SHG microscope (a, b, and c: dichroic beam splitters; d, e, and f: band-pass filters).

hydrothermal chemical method.[59] It was found that the photocatalytic activity of the Sn-doped (0.7 at%) β-Ga_2O_3 nanostructures significantly enhanced compared to that of intrinsic β-Ga_2O_3. Based on the results, the authors suggest the possible new opportunities to design highly effective β-Ga_2O_3-based photocatalysts for applications in environmental remediation, disinfection, and selective organic transformations.[59] However, despite the fact that Sn doping of Ga_2O_3 single crystals and thin films has been explored quite extensively in recent years, the fundamental aspects of Sn mixing into Ga_2O_3 inorganic compounds have not been considered much in the literature. Such a deeper understanding of the structural chemistry and structure−property correlation is the key to manipulate the materials for desired applications. Therefore, in the present work, we focused our efforts on understanding the functional relationship between the structure, chemical composition, band gap, and optical properties in Sn-mixed Ga_2O_3 compounds synthesized via the solid-state chemical reaction route. The impetus is to fill the knowledge gap in addition to demonstrating the unusual nonlinear optical activity, which appears as the effect of Sn addition, in Ga-Sn-O compounds compared to intrinsic Ga_2O_3. Furthermore, as presented and discussed in this study, understanding the detailed structural and optical properties as a function of Sn concentration enhances our ability to design the materials for practical device applications.

■ MATERIALS AND METHODS

Synthesis. The Sn-mixed Ga_2O_3 compounds were produced via the high-temperature, solid-state chemical reaction method. In order to obtain homogeneous compounds in the series of Sn-mixed Ga_2O_3 (referred to as Ga-Sn-O), high-purity Ga_2O_3 (99.99%) and SnO_2 (99.99%) powders were mixed thoroughly. The ratio for Sn was adjusted based on a balanced stoichiometry, following the chemical formula $Ga_{2-2x}Sn_xO_{3-\delta}$ (referred to as Ga-Sn-O), where x is the amount of Sn introduced. Compounds were prepared by varying the concentration of Sn in the range of $x = 0.0-0.3$. In the solid-state synthesis route adopted, we first initiated the process by grinding the powders using a mortar and pestle under a volatile liquid environment. This ensures homogeneous mixing and the formation of smaller-size particles. The mixture was calcined at a temperature closer to the melting point of the material. In this case, the mixed compound was heat-treated at 1100 °C for 12 h in a muffle furnace. The ramp rate used for heating and cooling was 5 °C/min. After calcination of the sample, the mixture was ground again by introducing polyvinyl acetate (PVA). Under the presence of PVA, the mixture was ground into a fine powder, which was then used to make pellets. The pellets were prepared by pressing the final Ga-Sn-O powder at 1.5 tons for 1 min, and they had dimensions of 8 mm diameter and 2 mm thickness.

The second stage of the Ga-Sn-O chemical compound synthesis involved a sintering process. The pellets were subjected to the second heat treatment, that is, sintering, at higher temperatures. The objective was to obtain a relatively dense material by closing the pores of the powder particles and also to eliminate any other defects that may have been present. The sintering temperature, which is typically higher than the calcination temperature, was set to 1350 °C for 12 h while maintaining the same ramp rate as that in the calcination. The final products, which are Ga-Sn-O materials with a variable Sn concentration (x), thus obtained, were subjected to characterization to understand the structure, composition, and electrochemical properties.

Characterization. *X-ray Diffraction.* The X-ray diffraction (XRD) analysis was performed on a Rigaku Smartlab diffractometer in zero-dimensional (0D) mode with a HyPix 3000 high energy resolution two-dimensional (2D) hybrid pixel array detector (HPAD). A trace amount of Ga-Sn-O powder was placed on a zero-diffraction plate to counter any diffraction peak arising from the sample holder. The X-ray source was set at the operating parameters of 44 kV and 40 mA. The step size was maintained at 0.02°. The diffraction data analysis or phase matching was carried out using the proprietary PDXL software.

Scanning Electron Microscopy. The Ga-Sn-O samples were used to study the morphological characteristics using the FEI Magellan 400 scanning electron microscope. Scanning electron microscopy (SEM) provides subnanometer spatial resolution. The samples were gold-coated (<5 nm thickness) before imaging to optimize the surface properties under SEM. The accelerating voltage was limited to 5 kV, and the working distance was maintained below 4 mm.

Energy-Dispersive X-ray Spectroscopy. To understand the phase separation and Sn chemistry, we performed energy-

https://doi.org/10.1021/acs.jpcc.1c04005
J. Phys. Chem. C 2021, 125, 20468−20481

dispersive X-ray spectroscopy (EDS) measurements on select compositions. For the purpose of EDS measurements, SEM (Hitachi High-Tech America, Inc., USA) was employed, while measurements were performed using the backscattered electron mode. An elemental compositional analysis was performed using EDS with the use of X-ray color mapping to allow for the approximate determination of elements present and their distribution characteristics.

Diffuse Reflectance Spectroscopy. To understand the optical behavior and to determine the band gap of these as-prepared Ga-Sn-O samples, diffuse reflectance spectroscopy was performed in a vertical photoexcitation configuration within a 60 mm integrating sphere, associated with a JASCO V-770 spectrometer with a single monochromator. Furthermore, a Kubelka−Munk function was derived from the diffuse reflectance data, which is proportional to the absorption coefficient of the same.

Nonlinear Optical Characterization—Second Harmonic Generation Microscopy. Second harmonic generation (SHG) imaging was performed using a home-built laser scanning nonlinear optical microscope (Figure 1).[60−62] A femtosecond Ti-sapphire laser (Mai Tai HP, Spectra-Physics) was used as the excitation source. A photomultiplier tube (PMT) with a band-pass filter (417−477 nm) was used to detect SHG signals. $Ga_{2-2x}Sn_xO_3$ samples with varying doping levels (x = 0.3, 0.15, 0.05, and 0) were prepared as loosely packed powders and were prepared for imaging by mounting between a glass slide and glass coverslip.

An area of 5 mm^2 was searched on each sample to locate SHG-active regions, which were then imaged again to obtain power- and polarization-dependent image series (power scans and polarization scans). Power scans were performed on SHG-active regions by capturing images using various laser powers from 1 to 100 mW in 5 mW increments or from 1 to 200 mW in 10 mW increments, depending on the intensity levels of SHG signals. To quantify the power dependence, mean values of SHG signals were plotted against laser powers in a double-log plot. Polarization scans were performed on the SHG regions by introducing a half-wave plate (HWP) into the excitation laser beam path (Figure 1) and rotating it to vary the electric field polarization direction of the incoming beam through 0 to 360° with increments of 10°. These polarization-dependent images were analyzed by selecting small regions showing SHG variations with the polarization angle, calculating the mean SHG intensity for these regions and plotting on polar axes with the angular axis for the angle of polarization and the radial axis for the SHG intensity.

Electrochemical Activity. The electrocatalytic activity of Ga-Sn-O toward hydrogen evolution reaction (HER) was evaluated using a three-electrode system with the Ag/AgCl reference electrode, the glassy carbon working electrode, and graphite as the counter electrode. Linear sweep voltammetry measurements were performed using a CHI 6273E potentiostat at a scan rate of 5 mV/s. To prepare the working electrode, a homogeneous mixture of sample (2 mg/mL) in 1:1 ratio of water and ethanol was prepared. Furthermore, 80 μL of 5 wt % Nafion 117 solution was mixed with the above-prepared solution and sonicated thoroughly. Finally, 20 μL of the above-prepared homogeneous mixture was drop-casted onto a freshly polished glassy carbon working electrode (3 mm diameter). The catalytic activity was investigated in the 0.5 M H_2SO_4 electrolyte solution. The potential was converted into the reversible hydrogen electrode (RHE) scale using the following equation:

$$E(\mathrm{RHE}) = E_{\mathrm{Ag/AgCl}} + 0.059\ \mathrm{pH} + E_{\mathrm{oAg/AgCl}} \quad (1)$$

where $E_{\mathrm{oAg/AgCl}}$ = 0.1976 V, and $E_{\mathrm{Ag/AgCl}}$ is the working potential.

RESULTS AND DISCUSSION

Crystal Structure and Phase Analysis. Figure 2 shows the crystal structures of Ga_2O_3 and SnO_2 with monoclinic and tetragonal lattice structures, respectively. These structural data may be useful to understand the present work on Ga-Sn-O compounds, especially the structural features derived from XRD. Figure 3 shows the XRD patterns of Ga-Sn-O compounds with a variable composition of Sn. For better understanding and comparison, the XRD peaks were identified and indexed to the monoclinic Ga_2O_3. It is evident that the Sn incorporation induces a secondary phase formation with increasing concentration. The secondary phase identified is SnO_2. The first instance of this SnO_2 secondary phase is noted for a Sn concentration of x = 0.15.

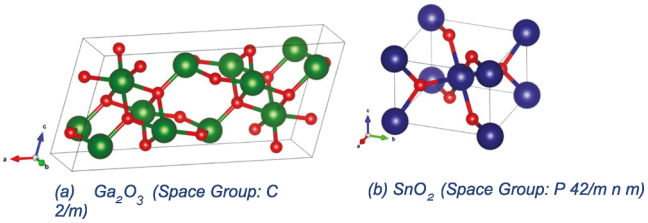

Figure 2. Crystal structures of (a) Ga_2O_3 and (b) SnO_2 with monoclinic and tetragonal lattice structures, respectively.

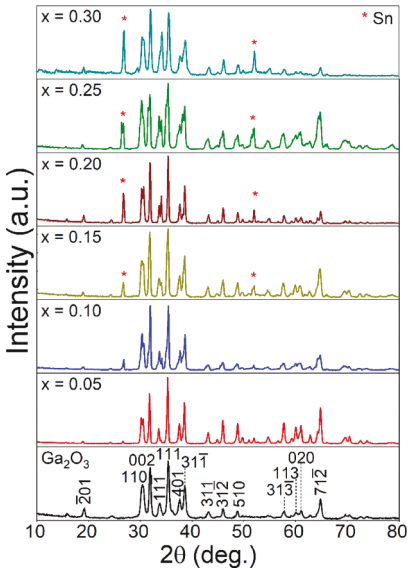

Figure 3. XRD patterns of the Ga-Sn-O compounds. The peaks due to Ga_2O_3 are as indicated. It is evident that the secondary phase formation occurs at a higher concentration of Sn. The peaks due to the secondary SnO_2 phase are indicated with asterisks.

The lattice parameters of the Ga-Sn-O compounds were calculated using the following equation:

https://doi.org/10.1021/acs.jpcc.1c04005
J. Phys. Chem. C 2021, 125, 20468−20481

$$\frac{1}{d^2} = \frac{1}{\sin^2\beta}\left(\frac{h^2}{a^2} + \frac{k^2\sin^2\beta}{b^2} + \frac{l^2}{c^2} - \frac{2hl\cos\beta}{ac}\right) \quad (2)$$

The lattice parameters of intrinsic Ga_2O_3 are as follows: a = 12.16 Å, b = 3.036 Å, and c = 5.78 Å. These lattice parameter values of intrinsic Ga_2O_3 are in reasonably good agreement with the literature.[19,35−37,6] For the highest concentration of Sn (x = 0.3), the calculated lattice parameters are as follows: a = 11.86 Å, b = 3.044 Å, and c = 5.75 Å. Ga_2O_3 exhibits pronounced polymorphism. The β-phase (β-Ga_2O_3), which is the most common phase, has been studied experimentally and theoretically to find the lattice parameters. β-Ga_2O_3 crystallizes in the monoclinic structure with a C2/m space group.[19] For Ga_2O_3, Kohn reported the following lattice parameters, which were determined experimentally: a = 12.23 Å, b = 3.04 Å, c = 5.80 Å, and β =103.7°.[63] In the same work, the calculated lattice parameters were as follows: a = 12.27 Å, b = 3.04 Å, c = 5.80 Å, and β =103.7°. A 0.3% difference from the experimental values was noted by Kohn et al.[63] Ahman et al.[64] reported the following lattice parameters: a = 12.21 Å, b = 3.037 Å, c = 5.798 Å, and β =103.83°; there is not much difference between these results. Thus, the comparison of the XRD data with the literature and indexing of the peaks noted indicate that the Ga-Sn-O compounds also crystallize in the monoclinic structure similar to undoped β-Ga_2O_3. However, such phase stabilization without any perturbation to the parent host structure occurs only at lower concentrations of Sn. At higher Sn concentrations, $x \geq 0.15$, the peaks due to the secondary SnO_2 phase occur in addition to the major contribution from the β-Ga_2O_3 phase. Thus, the Ga-Sn-O compounds exhibit the coexistence of monoclinic- and tetragonal-structured oxides of Ga and Sn, respectively. These results are in good agreement with recent reports on Sn-doped β-Ga_2O_3 nanomaterials synthesized using various chemical methods.[59,65] The more detailed account of the mixed-phase compounds is further probed using refinement procedures and analyses, which are presented and discussed subsequently.

The average crystallite size was obtained from the XRD data using the Scherrer equation:

$$D = 0.9\lambda B\cos\theta \quad (3)$$

where D, λ, B, and θ are the crystallite size, the wavelength of X-ray, the full width at half maximum, and the angle of the diffraction peak, respectively. The average grain size values followed a clear trend and decreased from ∼40 to ∼15 nm with increasing Sn concentration, that is, for variation in x values from 0.0 to 0.3. The effect of Sn incorporation on the overall chemistry can be understood based on the variation in the density of the Ga-Sn-O materials. The variation of the density of Ga-Sn-O compounds as a function of Sn is presented in Figure 4. The theoretical density, which is calculated based on the amount of Sn to obtain the final composition, is compared with the density calculated from the XRD data. Two important observations that can be noted from Figure 4 are as follows. A reasonably good agreement between the theoretical density and the calculated density of Ga-Sn-O compounds is the first. This observation is important as it reflects the structural quality of the materials synthesized and, perhaps, the chemical homogeneity in terms of Sn concentration across the oxide matrix or the entire material. A gradual, linear increase in density with increasing Sn concentration in Ga-Sn-O compounds is the second. This latter feature can be simply attributed to the fact that the heavier Sn atoms (118.69 amu) substitute for relatively lighter Ga atoms (69.72 amu), or more of the heavier Sn atoms are incorporated.

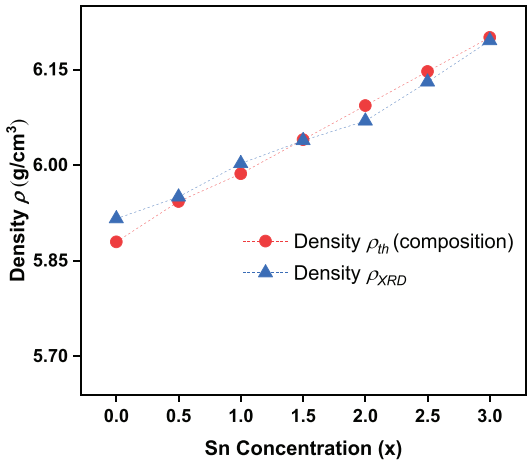

Figure 4. Variation of the density of the Ga-Sn-O compounds. A reasonably good agreement between the theoretical density, which is calculated based on the amount of Sn, and the density calculated from the XRD data can be seen. Also, a linear increase in density with increasing Sn concentration can be noted.

Rietveld Refinement. Rietveld refinement, which is often employed to understand the structure and phase identification, has been employed in this work to quantitatively understand the distinct phases present in mixed-phase Ga-Sn-O materials. Rietveld refinement was performed to simulate the corresponding XRD patterns and to specifically probe the SnO_2 secondary phase formation and quantification. The factors refined are the occupancy, lattice parameters, strain, crystallite size, scale factor, porosity, density, atomic position, B isotropy, background, zero-shift 2θ correction, anisotropic broadening, and preferred orientation. The best fit of the refinement was achieved by computing the peak positions, widths, and shapes using the least square procedure from the calculated and observed patterns. Figure 4 shows the Rietveld refined XRD patterns of the Ga-Sn-O compounds. It was noted that corroborating the XRD calculations, the material consists of two distinct phases, that is, the tetragonal phase for SnO_2 and the monoclinic phase for Ga_2O_3. The space groups of SnO_2 and Ga_2O_3 are P42/m n m and C2/m, respectively. Quantitatively, the initial composition where the SnO_2 tetragonal phase appears as a secondary phase is x = 0.15. The highest amount of SnO_2 phase formation occurs at x = 0.3, where the identified phase contributions are 88.08% of the monoclinic Ga_2O_3 phase and 11.92% of the tetragonal SnO_2 phase. The variation of the SnO_2 phase fraction with composition in the Ga-Sn-O materials is presented in Figure 5. The highest percentage of SnO_2 phase formation, particularly for x = 0.3, is evident from the prominent peaks of (110) and (121) in the XRD patterns. From refinement, the (011), (020), (111), and (120) peaks seem to be contributing significantly to quantify the SnO_2 phase present in the material as they gradually increase in intensity with increase in the concentration of Sn. Thus, the results from the refinement of these materials conclude that Sn mixing was able to retain the crystal structure of parent Ga_2O_3 at the initial stages of Sn incorporation, while randomly oriented tetragonal structure SnO_2 coexists with monoclinic Ga_2O_3 at higher concentrations.

https://doi.org/10.1021/acs.jpcc.1c04005
J. Phys. Chem. C 2021, 125, 20468−20481

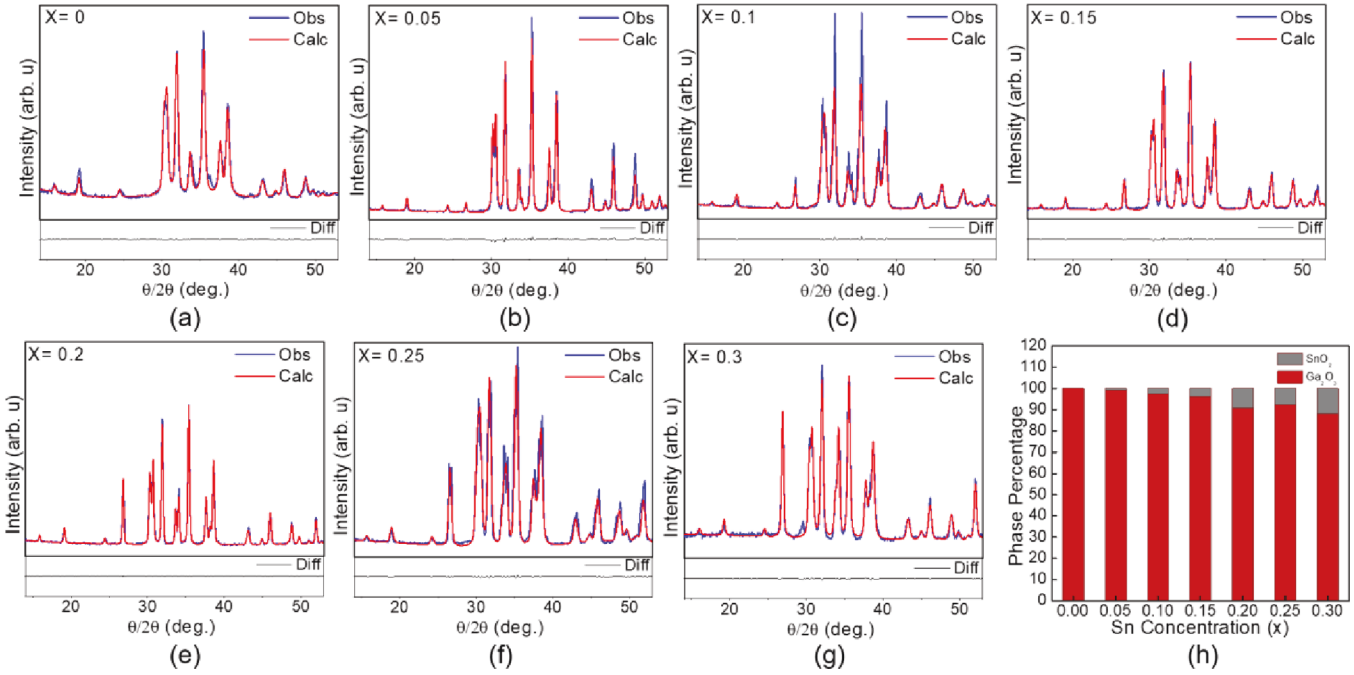

Figure 5. (a–g) Refined XRD patterns of the Ga-Sn-O materials. Data presented show the observed and calculated (Rietveld refinement) XRD patterns for all the Ga-Sn-O materials as a function of Sn concentration. (h) Phase fraction of Ga-Sn-O compounds. The respective fraction of the Ga_2O_3 host and SnO_2 secondary phases and their variation as a function of Sn concentration. The secondary phase formed in the Ga-Sn-O compounds as a result of Sn mixing becomes appreciable only at a higher concentration of Sn.

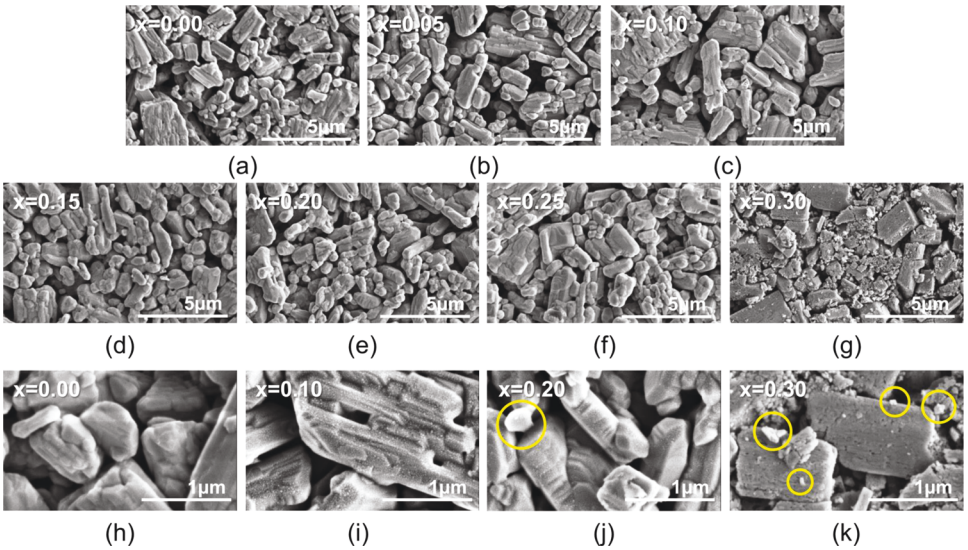

Figure 6. SEM images of the Ga-Sn-O materials as a function of Sn concentration. (a–g) SEM images of Ga-Sn-O compounds indicating the effect of Sn concentration on the morphology evolution. (h–k) High-resolution SEM images indicating the signature of SnO_2 phase evolution and segregation for higher Sn concentration in the Ga-Sn-O materials. x = 0.10 Sn concentration (i) shows tiny dots throughout the surface of the Ga_2O_3 crystals, whereas x = 0.20 onward, SnO_2 forms separate crystals outside the Ga_2O_3 matrix, shown inside yellow circles.

The strain in the Ga-Sn-O materials can be understood based on the interfacial phase modulation and associated structural distortion. Evidently, starting from pure β-Ga_2O_3, with increasing Sn concentration, a clear increasing trend of the overall strain is noted in structural characterization. The interplay among three different phenomena, such as interatomic replacement of Ga by Sn, interstitial placing of Sn atoms inside the β-Ga_2O_3 phase, and formation of separate crystalline grains of tetragonal SnO_2 and monoclinic β-Ga_2O_3, is responsible for this peculiar behavior. The first two phenomena are responsible for the formation of the strained β-Ga_2O_3 crystal phase. The last one usually results in crystal relaxation. Because of a much larger atomic size of Sn than Ga, it is natural that interatomic replacement or interstitial presence of Sn in the β-Ga_2O_3 phase is prone to strained crystal formation. However, there is a solubility limit of Sn in the β-Ga_2O_3 crystal structure. Beyond this limit, Sn segregates from the host crystal and stabilizes as SnO_2, which is clearly seen as a secondary phase (tetragonal structure) in the XRD analyses. Although the exact chemical composition at which the SnO_2 phase separates is slightly different from that in other studies, especially those reported for Sn-doped β-Ga_2O_3

https://doi.org/10.1021/acs.jpcc.1c04005
J. Phys. Chem. C 2021, 125, 20468−20481

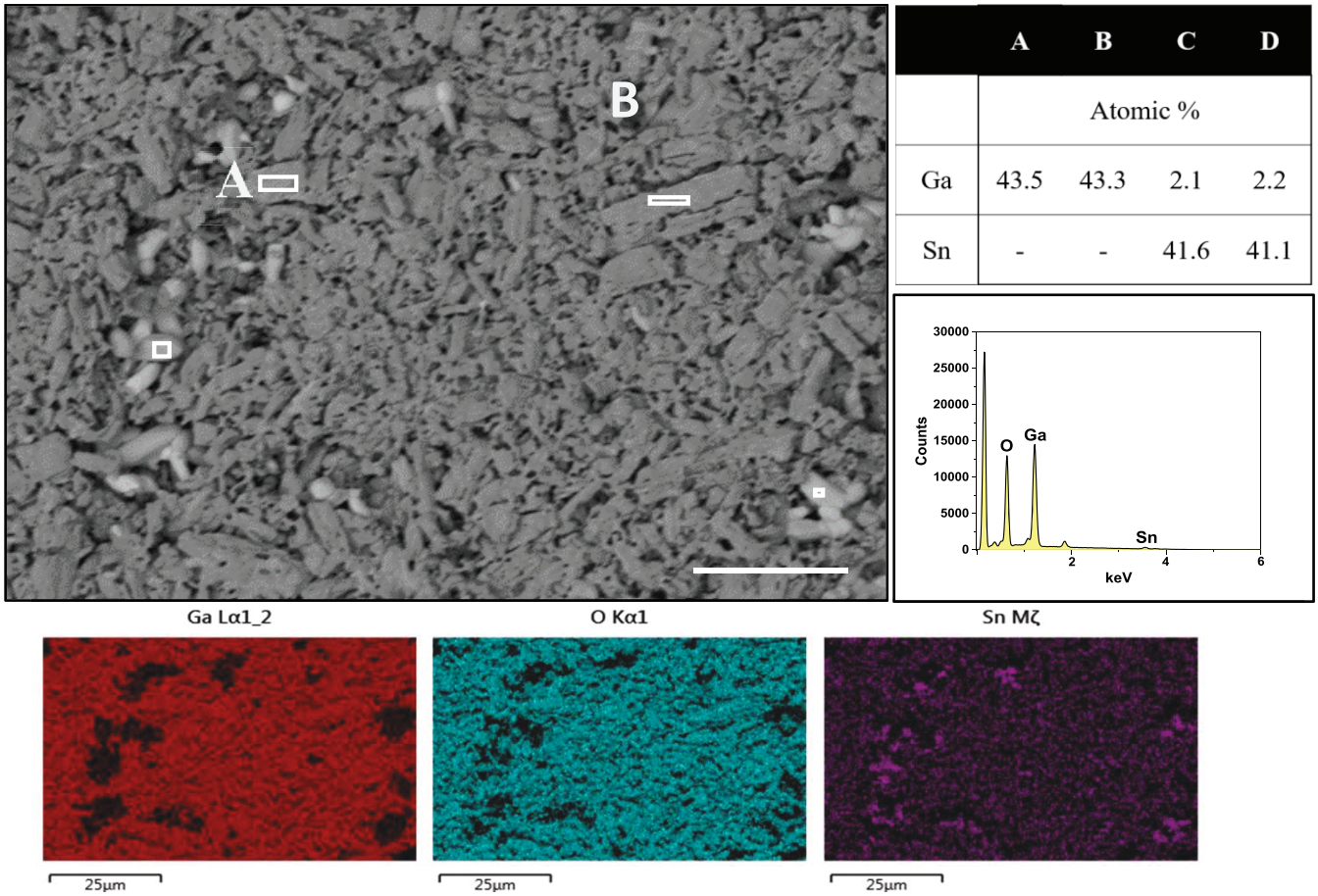

	A	B	C	D
	Atomic %			
Ga	43.5	43.3	2.1	2.2
Sn	-	-	41.6	41.1

Figure 7. EDS data of the Ga-Sn-O compounds. SEM image of the Ga-Sn-O composition with $x = 0.2$ at 3000× in the backscattering electron mode (upper panel) shows the elemental contrast. The marked regions of A, B, C, and D indicate the representation of Ga-oxide and Sn-oxide areas. It can be noted (Table, upper panel) that the Sn isolates form SnO_2 as a secondary phase. The EDS color mapping of the Ga, Sn, and O elements (lower panel) indicates the composition distribution of the respective elements.

nanomaterials synthesized using chemical[65] or hydrothermal[59] methods, our results closely agree with those reported in the literature.[53−55] Furthermore, Rietveld refinement of the corresponding $\theta/2\theta$ XRD scans also provides strong evidence for the presence of a separate SnO_2 phase along with β-Ga_2O_3, especially for $x \geq 0.15$. Thus, we believe that the coexistence of monoclinic-phase β-Ga_2O_3 and tetragonal-phase SnO_2 plays the key role and induces structural distortion, which further induces significant strain in the Ga-Sn-O materials. Such interfacial phase modulation-induced structural distortion strongly influences the optical and electrochemical properties of these Ga-Sn-O materials, as presented and discussed in subsequent sections. The goodness of fit for all the Rietveld refinements is <5, while the percentages of individual phases are approximated to the second decimal place.

Surface Morphology and Elemental Composition. The structural and crystallographic information, as presented and discussed in the aforementioned sections, of these complex Sn-mixed Ga_2O_3 inorganic compounds was subjected to further studies to gain insights into the morphological evolution as a function of the Sn content. Assertively, there is an evident signature in the SEM images for the formation of SnO_2 secondary phase with increasing Sn concentration. Dissociated SnO_2 crystals, which appeared as a secondary phase in XRD analyses, were found to be accumulated throughout the surface of host β-Ga_2O_3 grains. A clear difference in contrast is reflected in the SEM images shown in Figure 6 (images i and j in comparison with image h); these images provide evidence for such chemically induced surface segregation. Small molelike features appear with Sn incorporation. Owing to the larger crystal size of SnO_2, it is quite natural that the parasitic phase will try to come out of the host and try to accumulate along the circumference of the same. As we keep increasing the Sn concentration, further phase separation occurs, and small parasitic SnO_2 crystals start agglomerating to form larger SnO_2 grains, which can be visually distinguished from β-Ga_2O_3 with the help of color contrast in the SEM images. Finally, for a higher amount ($x = 0.3$) of Sn incorporation, duly sintered at an optimized temperature, there is prominent evidence of crack formation in the host β-Ga_2O_3 crystals (Figure 6, image k), which is the result of rigorous phase separation between β-Ga_2O_3 and SnO_2.

The EDS results and analyses provided direct evidence for Sn-oxide secondary phase formation. Figure 7 shows the EDS data of a representative sample, where $x = 0.2$. The Ga-Sn-O samples probed at various areas (spot analysis mode) to examine the composition distribution. As seen in the image, bright clusters of particles are visible throughout. These are believed to be SnO_2 particles. The areas marked A and B are proven to be β-Ga_2O_3 particles based on the ratio from the atomic percentage present. The areas marked as C and D seem

https://doi.org/10.1021/acs.jpcc.1c04005
J. Phys. Chem. C 2021, 125, 20468−20481

to be SnO_2 based on the ratio of the atomic percentages. In the color maps, the areas where Sn is present are clearly visible and show gaps on the Ga map. The elemental contrast between the particles allows the ability to differentiate between the different particles, where the Sn particles appear brighter. These areas are confirmed to be SnO_2 from the spot analysis. The color mapping shows a clear difference in the area between the Ga-enriched areas as compared to the Sn-enriched areas.

Optical Properties. The optical properties of the Sn-mixed Ga_2O_3 compounds were studied using diffuse reflectance spectroscopy. To investigate the interaction with incident photons under highly scattering medium or relatively opaque samples, this is the only way to optically probe the samples.[66,67] Figure 8 shows the optical characteristics of Ga-Sn-O compounds as a function of Sn concentration. It is evident from Figure 8 that as the Sn percentage increases, the band edge of the material shifts. However, the effective reduction in the band gap occurs until the Sn concentration is 0.25, at which point the band gap decreases drastically. In addition, the presence of an additional sub-band transition at a much lower energy value (3.6 eV) is prominent in the Ga-Sn-O compounds with the highest Sn concentration.

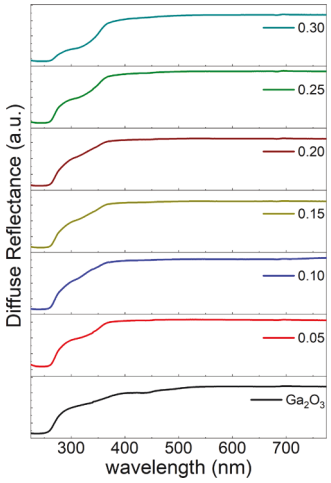

Figure 8. Diffuse reflectance spectra of the Ga-Sn-O samples as a function of Sn concentration.

To calculate the optical band gap of the Ga-Sn-O compounds, diffuse reflectance data were analyzed with the help of the Kubelka−Munk function,[68] which is defined as follows:

$$F(R) = \frac{K}{S} = \frac{(1 - R)^2}{2R} \tag{4}$$

Here, $F(R)$ represents the Kubelka−Munk function, which replicates a pattern similar to that of wavelength-dependent absorbance of the material, and K, S, and R are the absorption coefficient, the scattering coefficient, and reflectance, respectively. Figure 9 presents the corresponding wavelength-dependent $F(R)$ plots for each and every Ga-Sn-O sample and the procedure implemented to determine the band gap accurately. In this case, the modified Tauc equation has been implemented to calculate the band gap of the Ga-Sn-O materials.

$$\alpha \times h\upsilon = A(h\upsilon - E_g)^n \tag{5}$$

$$F(R) \times h\upsilon = A(h\upsilon - E_g)^n \tag{6}$$

Here, α, h, υ, E_g, $F(R)$, and A represent the absorption coefficient, Planck's constant, incident photon frequency, optical band gap, Kubelka−Munk function, and fitting constant, respectively. We used $n = 1/2$ for calculating the allowed direct transition energy in the electronic band structure. The Tauc plots (Figure 9), $[F(R)^* h\nu]^2$ vs $h\nu$, are typically used to determine the direct band gaps of Ga_2O_3-based compounds. In the present case of Ga-Sn-O compounds, the band gap values were calculated by extrapolating the linear

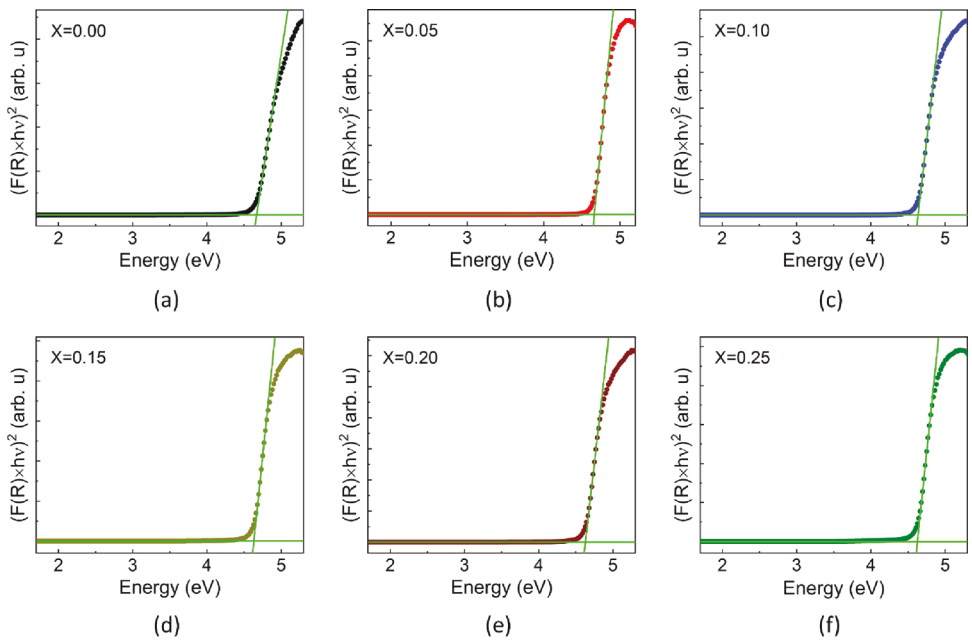

Figure 9. Tauc plots of the Ga-Sn-O materials. The plots were made using the Kubelka−Munk function, derived from the reflectance data, shown in Figure 8, of the corresponding Ga-Sn-O samples.

https://doi.org/10.1021/acs.jpcc.1c04005
J. Phys. Chem. C 2021, 125, 20468−20481

portion of these curves to zero absorption (x-axis), as shown in Figure 9. It can be noted that the band gap determined from these plots exhibits a gradual decrease with increasing Sn concentration.

The optical absorption behavior in these Ga-Sn-O materials becomes very interesting, particularly for a higher Sn content (x). To illustrate the scientific importance, we consider the data for the highest concentration (x = 0.3), as seen in Figure 10, which represent the Tauc plots of the Ga-Sn-O samples for

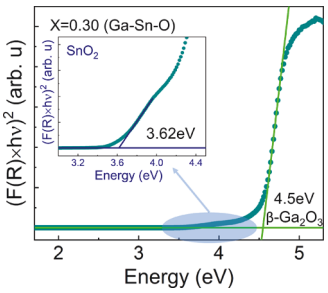

Figure 10. Tauc plots of the Ga-Sn-O samples with the highest Sn concentration (x = 0.30). β-Ga_2O_3-dominant phase shows band-edge absorption around 4.5 eV, whereas another secondary transition is seen at 3.62 eV, which corresponds to the SnO_2 crystals.

x = 0.30. Unlike the single-phase Ga-Sn-O materials (for $x \leq 0.15$), it is remarkable to note that the absorption data show two bands. The β-Ga_2O_3 dominant phase shows a strong band edge absorption at ~4.5 eV, which corresponds to the reduced band gap of β-Ga_2O_3. On the other hand, there is a sub-band transition (see, inset Figure 10) at lower energy. The Tauc plot analysis, as presented in the inset of Figure 10, indicates that the band gap is at 3.62 eV, which corresponds to the segregated SnO_2 phase. The variation in the band gap as a function of Sn concentration in the Ga-Sn-O compounds is presented in Figure 11.

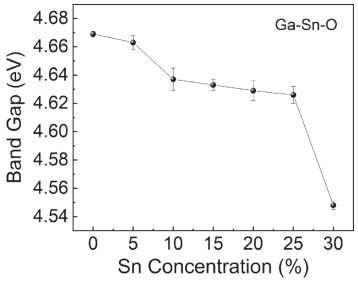

Figure 11. Variation of the band gap with Sn concentration in the Ga-Sn-O materials.

The chemistry behind the band gap variation (Figure 11) in the Ga-Sn-O compounds can be understood as follows. The band gap of pure Ga_2O_3 is ~4.75 eV, which is in good agreement with the literature values reported for Ga_2O_3 bulk or polycrystalline materials.[1−15] In intrinsic β-Ga_2O_3, the valence band edge is dominantly formed by the O-2p orbitals, while that of the conduction band is primarily formed by the Ga-4s orbitals. However, the effect of hybridization becomes the important process governing the electronic structure changes upon Sn incorporation. Based on the XRD data and related analyses, because the formation of single-phase compounds occurs for lower x values, the substitutional nature of Sn without disturbing the monoclinic structure of Ga_2O_3 is possible up to a certain level of Sn concentration. This can be understood from the considerations of the Shannon ionic radii of Ga and Sn. The ionic radii of Sn^{4+} (0.67 Å) ions closely match with those of Ga^{3+} (0.62 Å) ions. Therefore, Sn^{4+} ions can be substituted at the Ga site, which can replace Ga^{3+} ions in β-Ga_2O_3. In fact, based on the experimental and theoretical investigations, it is well established that in monoclinic β-Ga_2O_3, where Ga atoms occupy both octahedral and tetrahedral sites, Sn^{4+} ions prefer to substitute only those Ga ions in octahedral sites.[24,58,59,65,69] Varley et al. predicted such a sire preference for Sn^{4+} ions using the first-principles calculations.[24] Recently, Siah et al. performed advanced X-ray absorption studies, where two different possibilities in which Sn atoms can be incorporated into the monoclinic β-Ga_2O_3 host lattice were considered, and concluded that there the Sn^{4+} ions preferentially substitute Ga ions at the octahedral site.[69] Therefore, as revealed by the XRD data and refinement procedures, the Sn incorporation into β-Ga_2O_3 proceeds by the substitution of the dopant Sn^{4+} ions at the Ga^{3+} lattice sites. However, the difference in the ionic radii of Sn^{4+} and Ga^{3+} induces lattice distortion, as noted in XRD analyses. Under such conditions, and as permitted by the solubility limit, no perturbation to the parent crystal structure, that is, the monoclinic structure of β-Ga_2O_3, is seen for Sn incorporation. Therefore, for single-phase Ga-Sn-O compounds, the electronic structure changes occur because of the Sn ions substituted for Ga ions. As such, the redshift observed in the band gap can be explained based on the sp-d exchange interaction (see, Figure 11) between the valance-band electrons and localized d electrons of Sn in Ga_2O_3.

Nonlinear Optical Activity. All four Ga-Sn-O showed a few, small (5−30 μm size) SHG-active regions distributed sparsely throughout each sample. Figure 12 is a representative image.

As a second-order nonlinear optical process, SHG intensity is proportional to the square of the laser intensity incident on the sample. Further supporting the interpretation of the observed signal as SHG, double-log plots of SHG intensity vs power (Figure 13) show a maximum slope in the range of 1.6−2 in the unsaturated region of the curves, as expected for the quadratic SHG−power relationship. The presence of the SHG

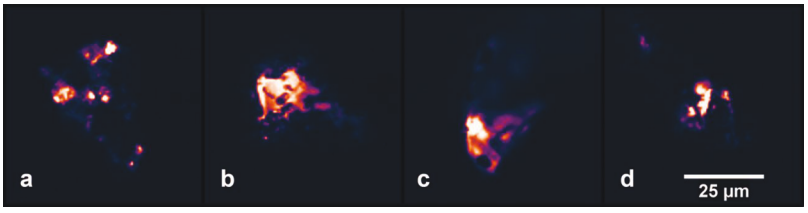

Figure 12. Representative SHG microscopic images. (a) x = 0.3, (b) x = 0.15, (c) x = 0.05, and (d) x = 0.

https://doi.org/10.1021/acs.jpcc.1c04005
J. Phys. Chem. C 2021, 125, 20468−20481

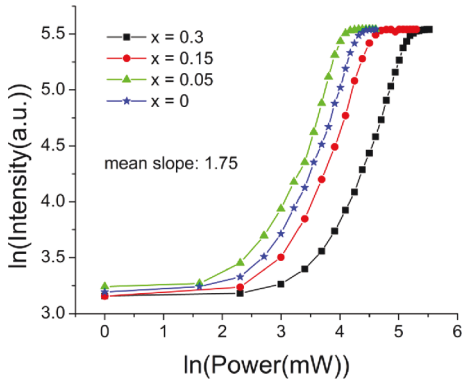

Figure 13. Double-log plot of SHG intensity vs laser power of the $Ga_{2-2x}S_{nx}O_3$ series (x = 0.3, x = 0.15, x = 0.05, and x = 0).

signal suggests that these isolated regions contain material of a noncentrosymmetric structure, while the surrounding material is centrosymmetric. SHG could also occur if the material has a broad centrosymmetric structure but a broken symmetry locally within the SHG regions.[70,71] Because β-Ga_2O_3 crystals are in the monoclinic C2/m space group, most likely, these SHG-active regions are due to the local broken symmetry.

The SHG signal depends on the incoming laser electric direction and the crystal structure orientation. Therefore, while rotating the laser beam polarization, the SHG signal intensity changes accordingly. Two distinct shapes (dipolar and quadrupolar) were observed in such SHG polar plots (Figure 14). The quadrupolar plots generally show two strong lobes and two weak lobes perpendicular to the axis of the strong lobes. As demonstrated in an earlier work, the SHG polar image can resolve the wurtzite (dipole) and zinc blende (quadrupole) phases on a single GaAs nanowire.[72,73] Such varying polar plots indicate varying local symmetries/phases of Ga-Sn-O samples. Experimental studies on local crystal structures and theoretical investigations of local $\chi^{(2)}$ nonlinear susceptibility tensor can explain this interesting phenomenon.

Hydrogen Evolution Reaction. Transition/post-TM-oxide-based catalysts are now attracting attention for efficient energy conversions, especially for hydrogen evolution reaction (HER), because of the advantages of compositional diversity, flexible tunability, low cost, and abundant availability.[73] Among them, Ga_2O_3-based materials have gained attraction as photocatalysts because of their wide band gap, but their application as electrocatalysts still remains less explored. Generally, the performance of an electrocatalyst is greatly influenced by the active site density via the incorporation of dopant material, by introducing an interstitial defect, or by enhancing the surface area. Previous studies indicate that Sn doping can enhance the electrocatalytic properties because of improved active sites and accelerated electron transfer.[74,75] Here, we have investigated the catalytic activity of different percentages of Sn doping in Ga_2O_3 toward HER. Figure 15a represents the HER activity of the as-synthesized catalysts, which was investigated using a three-electrode setup in a 0.5 M H_2SO_4 medium. As evident from the figure, the pristine Ga_2O_3 did not exhibit any electrocatalytic activity in the given range similar to the previous reports.[34,35] However, all Sn-doped samples demonstrated considerable electrocatalytic performance with the highest activity demonstrated by GaSnO-15%, with an onset potential of −0.71 V and an overpotential of −0.80 V for 20 mA/cm^2. It is important to note that the dopant percentages of Sn play a crucial role in enhancing the HER performance of the materials prepared. The increase in

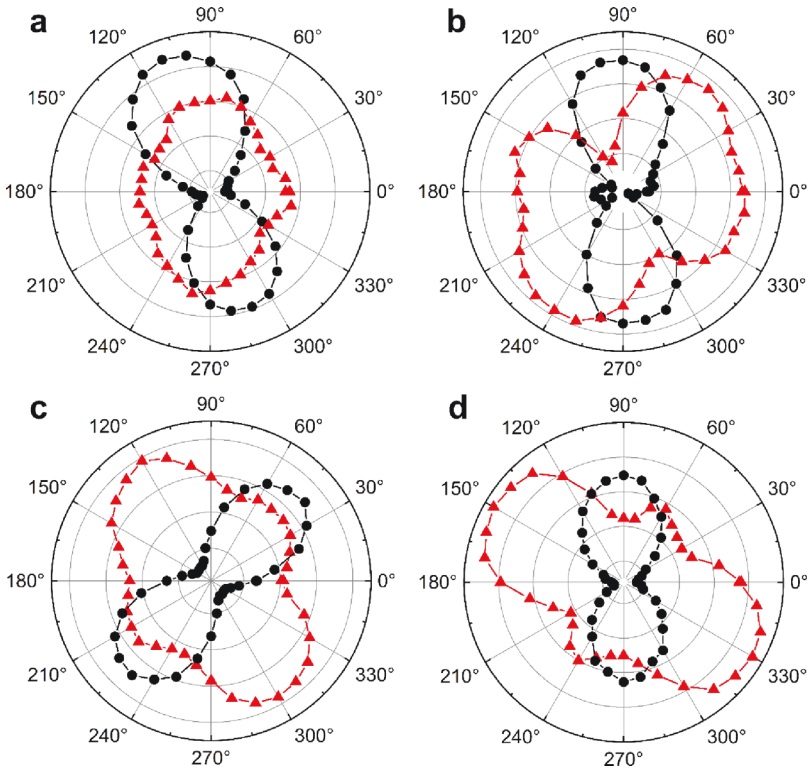

Figure 14. Polar plot of SHG intensity vs laser polarization. The distance from the origin represents SHG signal intensity, and the polar angle represents electric-field polarization. (a) x = 0.3, (b) x = 0.15, (c) x = 0.05, and (d) x = 0.

https://doi.org/10.1021/acs.jpcc.1c04005
J. Phys. Chem. C 2021, 125, 20468−20481

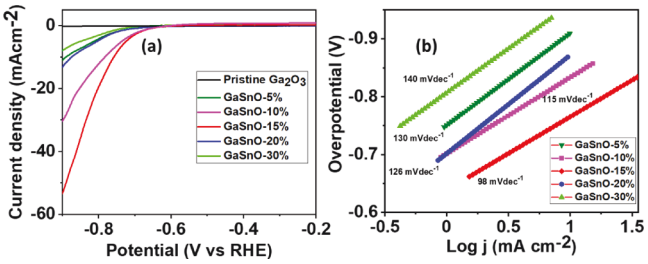

Figure 15. (a) Linear sweep voltammetry curves in the 0.5 M H_2SO_4 solution at a scan rate of 5 mV/s and (b) Tafel plots of Ga_2O_3 with different Sn-doping ratios.

the dopant percentage from 5 to 15% increases the number of active sites in the sample as well as its conductivity, resulting in enhancement in the observed catalytic activity. However, as the dopant percentage was increased beyond 15%, we observe a decrease in the electrocatalytic performance. This can be attributed to the structural changes in the sample, as apparent from the phase separation observed in the XRD data.

It is well known that the value of the Tafel slope has an important influence on the HER as it determines the rate of the reaction. Hence, to gain further insight into the catalytic performance, Tafel slopes of all the catalysts were calculated using the following equation:

$$\eta = a + b \log|J| \tag{7}$$

where η is the overpotential, b is the Tafel slope, and J is the current density. An electrocatalytic material with a smaller value of the Tafel slope is considered a better electrocatalyst because it increases hydrogen generation with a higher rate and an increase in the potential. The lowest Tafel slope is exhibited by GaSnO-15% with a value of 98 mV/dec, confirming its superior activity as well as better catalytic kinetics over other dopant percentages (Figure 15b). Based on the above-mentioned analysis, the appreciable HER performance of Sn-doped Ga_2O_3 with an optimum dopant percentage can be attributed to the increased number of active sites as well as the conductivity of the sample.

Finally, to summarize the findings and provide a road map to consider cation-doped β-Ga_2O_3 for practical applications, a schematic diagram explaining the effect of Sn^{4+} is presented in Figure 16. In the monoclinic unit cell of Ga_2O_3, Ga occupies either with the octahedrally coordinated oxygen or the tetrahedrally coordinated oxygen. On the other hand, oxygen

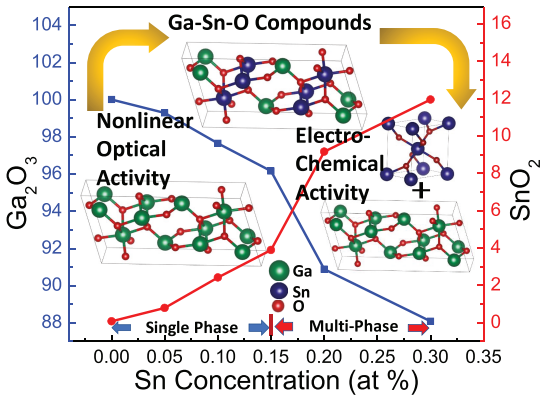

Figure 16. Schematic diagram explaining the effect of Sn^{4+} ions on the phase evolution, solubility, and properties of Ga_2O_3.

assumes three different lattice sites in distorted cubic close-packed arrangement around Ga sites. When doped, mixed, or alloyed, depending on the solubility limit of the foreign ion such as Sn into Ga_2O_3, the Sn ions will preferentially substitute Ga ions at the octahedral sites and provide efficient means to manipulate the structure and electronic properties. Thus, as seen in this case, when Sn ions substitute at the Ga site and form the single-phase Ga-Sn-O compounds, the materials become nonlinear-optical-active as well as electrochemical-active. At higher Sn concentrations, Ga_2O_3−SnO_2 composite formation occurs because of the segregation of the secondary SnO_2 phase. Thus, the solubility limit of Sn in Ga_2O_3 is very limited; however, this is already more than sufficient to play with chemical tuning to tailor the electronic structure as well as optical and electrochemical properties. While there was some indication in the literature that Sn doping into Ga_2O_3 can improve the photocatalytic activity,[59,65] the nonlinear optical activity of such compounds has not been observed or reported earlier. First, we consider the electrochemical activity in terms of the HER reaction. Clearly, the demonstrated activity in the Ga-Sn-O compounds for Sn-incorporation is the signature of chemical composition-induced electrochemical activity because such activity was absent in intrinsic Ga_2O_3. However, although it improved with increasing Sn concentration, the deterioration of the electrochemical activity at higher Sn concentrations ($x \geq 0.15$) clearly indicates that it is not only dependent on the Sn-incorporation but also depends on the phase. Because the onset of the secondary phase and interfacial modulation is evident at $x \geq 0.15$ in XRD and refinement studies, we believe that the single-phase compounds with a clear Sn solubility can result in better HER activity, while multiphase materials deteriorate. Furthermore, comparison of our results with those of recent work on Sn-doped Ga_2O_3 nanomaterials prepared using the hydrothermal method[59] and their photocatalytic activity evaluated by methylene blue degradation under ultraviolet light (254 nm) irradiation also indicate a similar implication. In Sn-doped Ga_2O_3 nanomaterials, the photocatalytic activity of the Sn-doped (0.7 at%) β-Ga_2O_3 nanostructures is significantly enhanced compared to that of intrinsic β-Ga_2O_3 nanostructures.[59] Excessive Sn concentrations (exceeding 2.2 at%) above the solid solubility limit of Sn in β-Ga_2O_3 nanostructures lead to SnO_2 precipitation, which degrades the photocatalytic efficiency in the β-Ga_2O_3 nanostructures.[59] Thus, it appears that the Sn solubility and single-phase compound formation are quite important from the electrochemical or photocatalysis point of view.

We now turn our attention to the nonlinear optical activity in Ga-Sn-O compounds. Unlike the electrochemical or photocatalytic properties, where the single-phase materials and Sn solubility are important, the SHG activity is observed to improve as Sn incorporation progresses. In fact, chemical composition tuning to the extent of realizing two-phase materials seems to be more effective in terms of nonlinear optical activity. Perhaps, the interfacial modulation of monoclinic (Ga_2O_3) and tetragonal (SnO_2) structures induce distortion, which in turn can break the centro-symmetry, leading to the observed SHG activity, which may be highly beneficial for applications in photonics. Also, the emerging applications of Ga_2O_3 and its related compounds are continuous, which is a strong indication for future novel technology development. For instance, recent studies hint at the possibility of large-area inorganic−organic thermoelectrics by means of controlled growth and tailoring the properties at

https://doi.org/10.1021/acs.jpcc.1c04005
J. Phys. Chem. C 2021, 125, 20468−20481

the molecular scale in Ga/Ga_2O_3 compounds. Notably, while there is a significant interest in overcoming the technological challenges in the design and development of cost-effective large-area inorganic−organic thermoelectrics, previous studies[13,14] warrant considering such materials for further development. While this is just one example we considered, we believe that the nonlinear optical activity can be further explored by means of rational design and development, especially by considering chemical composition tuning and various architectures of materials, such as nanoassemblies and core-shell structures of phases.

■ SUMMARY AND CONCLUSIONS

Summarizing the current study, we demonstrated the unexpected nonlinear optical activity in addition to the electrochemical/catalytic activity in Sn-incorporated Ga_2O_3. The structure, morphology, and chemical composition dependencies of the optical and electrochemical properties of Ga-Sn-O materials demonstrated in this work as a function of Sn incorporation can be advantageous for designing materials with tunable properties and performance. The Sn-incorporated Ga_2O_3 compounds prepared using the high-temperature solid-state chemical reaction method indicate that the chemical composition dependence allows for obtaining the single-phase and two-phase materials. The structural chemistry, morphology, and optical and electrochemical characterization demonstrate that the interplay between three fundamental phenomena of chemical origin is the key to derive tunable functional properties. The chemical phenomena are as follows: (a) Sn^{4+} incorporation proceeds preferentially to substitute Ga ions at the octahedral sites, leading to single-phase Ga-Sn-O materials; (b) substitutional or interstitial Sn incorporation and islanding of small, independent SnO_2 crystalline phases in parallel with the host β-Ga_2O_3 phase; (c) composite formation, where monoclinic β-Ga_2O_3 and tetragonal SnO_2 coexists. The solubility limit of Sn intermixing appears to be $x = 0.15$, beyond which there is a demonstrated evidence in XRD, SEM, and optical studies for self-sustained SnO_2 tetragonal-phase formation inside the monoclinic β-Ga_2O_3 host. The first two occurrences affect the strain balance and impurity incorporation inside the host matrix, resulting in broadening/shifting of the XRD peak, shifting of the optical band gap, increase of the effecting donor state, enhancement of the density of electrochemically activated sites, breaking of the local structural symmetry, and so forth. The last phenomenon forms separate crystalline phases with a relaxed strain value, but at the cost of breached-porous host matrix. From the abovementioned experimental evidence, it has been established that $x = 0.15$ is the optimum Sn fraction, where mainly substitutional and interstitial Sn incorporation dominates and gradual improvement in both SHG and catalytic hydrogen evolution is observed. These two multidimensional characteristics and functionalities open up a path for realizing complex microdevices with photomultiplication-assisted photoelectrochemical activity and further opportunities to design materials for photonics and optoelectronics. We plan to pursue the optoelectronic properties and design and development of photodetectors by making thin films of Ga-Sn-O compounds in the near future.

■ AUTHOR INFORMATION

Corresponding Author

C. V. Ramana − *Center for Advanced Materials Research (CMR) and Department of Mechanical Engineering, University of Texas at El Paso, El Paso, Texas 79968, United States;* orcid.org/0000-0002-5286-3065; Email: rvchintalapalle@utep.edu

Authors

Guillermo Gutierrez − *Center for Advanced Materials Research (CMR) and Department of Mechanical Engineering, University of Texas at El Paso, El Paso, Texas 79968, United States*

Emma M. Sundin − *Center for Advanced Materials Research (CMR), University of Texas at El Paso, El Paso, Texas 79968, United States; Department of Metallurgical, Materials and Biomedical Engineering, University of Texas at El Paso, El Paso, Texas 79968, United States*

Paul Gaurav Nalam − *Center for Advanced Materials Research (CMR) and Department of Mechanical Engineering, University of Texas at El Paso, El Paso, Texas 79968, United States*

Vishal Zade − *Center for Advanced Materials Research (CMR) and Department of Mechanical Engineering, University of Texas at El Paso, El Paso, Texas 79968, United States*

Rebecca Romero − *Center for Advanced Materials Research (CMR), University of Texas at El Paso, El Paso, Texas 79968, United States; Department of Metallurgical, Materials and Biomedical Engineering, University of Texas at El Paso, El Paso, Texas 79968, United States*

Aruna N Nair − *Department of Chemistry and Biochemistry, University of Texas at El Paso, El Paso, Texas 79968, United States*

Sreeprasad Sreenivasan − *Department of Chemistry and Biochemistry, University of Texas at El Paso, El Paso, Texas 79968, United States;* orcid.org/0000-0002-5728-0512

Debabrata Das − *Center for Advanced Materials Research (CMR), University of Texas at El Paso, El Paso, Texas 79968, United States;* orcid.org/0000-0003-4326-6805

Chunqiang Li − *Department of Physics, University of Texas at El Paso, El Paso, Texas 79968, United States;* orcid.org/0000-0003-1220-1611

Complete contact information is available at: https://pubs.acs.org/10.1021/acs.jpcc.1c04005

Notes

The authors declare no competing financial interest.

■ ACKNOWLEDGMENTS

The authors acknowledge, with pleasure, support from the National Science Foundation (NSF) with NSF-PREM grant #DMR-1827745. This material is also based upon the work supported by the Air Force Office of Scientific Research under award number FA9550-18-1-0387. However, any opinions, findings, and conclusions or recommendations expressed in this material are those of the author(s) and do not necessarily reflect the views of the United States Air Force.

■ REFERENCES

(1) Farvid, S. S.; Wang, T.; Radovanovic, P. V. Colloidal gallium indium oxide nanocrystals: a multifunctional light-emitting phosphor

broadly tunable by alloy composition. *J. Am. Chem. Soc.* **2011**, *133*, 6711−6719.

(2) Castro-Fernández, P.; Blanco, M. V.; Verel, R.; Willinger, E.; Fedorov, A.; Abdala, P. M.; Müller, C. R. Atomic-Scale Insight into the Structure of Metastable γ-Ga_2O_3 Nanocrystals and their Thermally-Driven Transformation to β-Ga_2O_3. *J. Phys. Chem. C* **2020**, *124*, 20578−20588.

(3) Makeswaran, N.; Das, D.; Zade, V.; Gaurav, P.; Shutthanandan, V.; Tan, S.; Ramana, C. V. Size- and Phase-Controlled Nanometer-Thick β-Ga2O3Films with Green Photoluminescence for Optoelectronic Applications. *ACS Appl. Nano Mater.* **2021**, *4*, 3331.

(4) Nagarajan, L.; De Souza, R. A.; Samuelis, D.; Valov, I.; Börger, A.; Janek, J.; Becker, K.-D.; Schmidt, P. C.; Martin, M. A Chemically Driven Insulator-Metal Transition in Non-Stoichiometric and Amorphous Gallium Oxide. *Nat. Mater.* **2008**, *7*, 391−398.

(5) Su, J.; Guo, R.; Lin, Z.; Zhang, S.; Zhang, J.; Chang, J.; Hao, Y. Unusual Electronic and Optical Properties of Two-Dimensional Ga2O3Predicted by Density Functional Theory. *J. Phys. Chem. C* **2018**, *122*, 24592−24599.

(6) Wang, T.; Farvid, S. S.; Abulikemu, M.; Radovanovic, P. V. Size-tunable phosphorescence in colloidal metastable γ-Ga_2O_3 nanocrystals. *J. Am. Chem. Soc.* **2010**, *132*, 9250−9252.

(7) Kim, J.; Mastro, M. A.; Tadjer, M. J.; Kim, J. Heterostructure WSe_2-Ga_2O_3 Junction Field-Effect Transistor for Low-Dimensional High-Power Electronics. *ACS Appl. Mater. Interfaces* **2018**, *10*, 29724−29729.

(8) Liang, H.; Cui, S.; Su, R.; Guan, P.; He, Y.; Yang, L.; Chen, L.; Zhang, Y.; Mei, Z.; Du, X. Flexible X-ray Detectors Based on Amorphous Ga_2O_3 Thin Films. *ACS Photonics* **2019**, *6*, 351−359.

(9) Li, K. H.; Alfaraj, N.; Kang, C. H.; Braic, L.; Hedhili, M. N.; Guo, Z.; Ng, T. K.; Ooi, B. S. Deep-Ultraviolet Photodetection Using Single-Crystalline β-Ga_2O_3/NiO Heterojunctions. *ACS Appl. Mater. Interfaces* **2019**, *11*, 35095−35104.

(10) Qiao, B.; Zhang, Z.; Xie, X.; Li, B.; Li, K.; Chen, C.; Zhao, H.; Liu, K.; Liu, L.; Shen, D. Avalanche Gain in Metal−Semiconductor−Metal Ga_2O_3 Solar-Blind Photodiodes. *J. Phys. Chem. C* **2019**, *123*, 18516−18520.

(11) Bhuiyan, A. F.; Feng, Z.; Johnson, J. M.; Huang, H. L.; Hwang, J.; Zhao, H. MOCVD Epitaxy of Ultrawide Bandgap β-$(Al_xGa_{1-x})_2O_3$ with High-Al Composition on (100) β-Ga_2O_3 Substrates. *Cryst. Growth Des.* **2020**, *20*, 6722−6730.

(12) Pratiyush, A. S.; Krishnamoorthy, S.; Kumar, S.; Xia, Z.; Muralidharan, R.; Rajan, S.; Nath, D. N. Demonstration of zero bias responsivity in MBE grown β-Ga_2O_3 lateral deep-UV photodetector. *Jpn. J. Appl. Phys.* **2018**, *57*, No. 060313.

(13) Park, S.; Yoon, H. J. New Approach for large-area thermoelectric junctions with a liquid eutectic gallium−indium electrode. *Nano Lett.* **2018**, *18*, 7715−7718.

(14) Simeone, F. C.; Yoon, H. J.; Thuo, M. M.; Barber, J. R.; Smith, B.; Whitesides, G. M. Defining the value of injection current and effective electrical contact area for EGaIn-based molecular tunneling junctions. *J. Am. Chem. Soc.* **2013**, *135*, 18131−18144.

(15) Roy, S.; Mallesham, B.; Zade, V. B.; Martinez, A.; Shutthanandan, V.; Thevuthasan, S.; Ramana, C. V. Correlation between Structure, Chemistry, and Dielectric Properties of Iron-Doped Gallium Oxide ($Ga_{2-x}Fe_xO_3$). *J. Phys. Chem. C* **2018**, *122*, 27597−27607.

(16) Higashiwaki, M.; Sasaki, K.; Kuramata, A.; Masui, T.; Yamakoshi, S. Gallium oxide (Ga_2O_3) metal-semiconductor field-effect transistors on single-crystal β-Ga_2O_3 (010) substrates. *Appl. Phys. Lett.* **2012**, *100*, No. 013504.

(17) Higashiwaki, M.; Sasaki, K.; Murakami, H.; Kumagai, Y.; Koukitu, A.; Kuramata, A.; Masui, T.; Yamakoshi, S. Recent progress in Ga_2O_3 power devices. *Semicond. Sci. Technol.* **2016**, *31*, No. 034001.

(18) Pearton, S. J.; Yang, J.; Cary, P. H., IV; Ren, F.; Kim, J.; Tadjer, M. J.; Mastro, M. A. A review of Ga_2O_3 materials, processing, and devices. *Appl. Phys. Rev.* **2018**, *5*, No. 011301.

(19) Geller, S. Crystal Structure of β-Ga_2O_3. *J. Chem. Phys.* **1960**, *33*, 676−684.

(20) Víllora, E. G.; Shimamura, K.; Yoshikawa, Y.; Ujiie, T.; Aoki, K. Electrical conductivity and carrier concentration control in β-Ga_2O_3 by Si doping. *Appl. Phys. Lett.* **2008**, *92*, 202120.

(21) Zhang, F.; Arita, M.; Wang, X.; Chen, Z.; Saito, K.; Tanaka, T.; Nishio, M.; Motooka, T.; Guo, Q. Toward controlling the carrier density of Si doped Ga_2O_3 films by pulsed laser deposition. *Appl. Phys. Lett.* **2016**, *109*, 102105.

(22) Leedy, K. D.; Chabak, K. D.; Vasilyev, V.; Look, D. C.; Mahalingam, K.; Brown, J. L.; Green, A. L.; Bowers, C. T.; Crespo, A.; Thomson, D. B.; Jessen, G. H. Si content variation and influence of deposition atmosphere in homoepitaxial Si-doped β-Ga2O3films by pulsed laser deposition. *APL Materials* **2018**, *6*, 101102.

(23) Peelaers, H.; Van de Walle, C. Doping of Ga_2O_3 with transition metals. *Phys. Rev. B* **2016**, *94*, No. 195203.

(24) Varley, J. B.; Weber, J. R.; Janotti, A.; Walle, C. G. V. D. Oxygen vacancies and donor impurities in β-Ga_2O_3. *Appl. Phys. Lett.* **2010**, *97*, 142106.

(25) Peelaers, H.; Lyons, J. L.; Varley, J. B.; Walle, C. G. V. D. Deep acceptors and their diffusion in Ga_2O_3. *APL Mater.* **2019**, *7*, No. 022519.

(26) Wang, X.; Shen, S.; Jin, S.; Yang, J.; Li, M.; Wang, X.; Han, H.; Li, C. Effects of Zn^{2+} and Pb^{2+} dopants on the activity of Ga_2O_3-based photocatalysts for water splitting. *Phys. Chem. Chem. Phys.* **2013**, *15*, 19380−19386.

(27) Tatsumi, H.; Teramura, K.; Huang, Z.; Wang, Z.; Asakura, H.; Hosokawa, S.; Tanaka, T. Enhancement of CO Evolution by Modification of Ga_2O_3 with Rare Earth Elements for the Photocatalytic Conversion of CO_2 by H_2O. *Langmuir* **2017**, *33*, 13929−13935.

(28) Zhang, W.; Naidu, B. S.; Ou, J. Z.; O'Mullane, A. P.; Chrimes, A. F.; Carey, B. J.; Wang, Y.; Tang, S. Y.; Sivan, V.; Mitchell, A.; Bhargava, S. K.; Kalantar-Zadeh, K. Liquid metal/metal oxide frameworks with incorporated Ga_2O_3 for photocatalysis. *ACS Appl. Mater. Interfaces* **2015**, *7*, 1943−1948.

(29) Syed, N.; Zavabeti, A.; Mohiuddin, M.; Zhang, B.; Wang, Y.; Datta, R. S.; Atkin, P.; Carey, B. J.; Tan, C.; van Embden, J.; Chesman, A. S. R.; Ou, J. Z.; Daeneke, T.; Kalantar-zadeh, K. Sonication-assisted synthesis of gallium oxide suspensions featuring trap state absorption: test of photochemistry. *Adv. Funct. Mater.* **2017**, *27*, No. 1702295.

(30) Tien, L.-C.; Chen, W.-T.; Ho, C.-H. Enhanced Photocatalytic Activity in β-Ga_2O_3 Nanobelts. *J. Am. Ceram. Soc.* **2011**, *94*, 3117−3122.

(31) Layek, A.; Yildirim, B.; Ghodsi, V.; Hutfluss, L. N.; Hegde, M.; Wang, T.; Radovanovic, P. V. Dual europium luminescence centers in colloidal Ga_2O_3 nanocrystals: controlled in situ reduction of Eu (III) and stabilization of Eu (II). *Chem. Mater.* **2015**, *27*, 6030−6037.

(32) Rubio, E. J.; Mates, T. E.; Manandhar, S.; Nandasiri, M.; Shutthanandan, V.; Ramana, C. V. Tungsten Incorporation into Gallium Oxide: Crystal Structure, Surface and Interface Chemistry, Thermal Stability, and Interdiffusion. *J. Phys. Chem. C* **2016**, *120*, 26720−26735.

(33) Dakhel, A. A. Structural, optical, and opto-dielectric properties of W-doped Ga_2O_3 thin films. *J. Mater. Sci.* **2011**, *47*, 3034−3039.

(34) Bandi, M.; Zade, V.; Roy, S.; Nair, A. N.; Seacat, S.; Sreenivasan, S.; Shutthanandan, V.; Van de Walle, C. G.; Peelaers, H.; Ramana, C. V. Effect of Titanium Induced Chemical Inhomogeneity on Crystal Structure, Electronic Structure, and Optical Properties of Wide Band Gap Ga_2O_3. *Cry. Growth Des.* **2020**, *20*, 1422−1433.

(35) Mallesham, B.; Roy, S.; Bose, S.; Nair, A. N.; Sreenivasan, S.; Shutthanandan, V.; Ramana, C. V. Crystal Chemistry, Band-Gap Red Shift, and Electrocatalytic Activity of Iron-Doped Gallium Oxide Ceramics. *ACS Omega* **2020**, *5*, 104−112.

(36) Zade, V.; Mallesham, B.; Shantha-Kumar, S.; Bronson, A.; Ramana, C. V. Interplay between solubility limit, structure, and optical properties of tungsten-doped Ga_2O_3 compounds synthesized by a two-step calcination process. *Inorg. Chem.* **2019**, *58*, 3707−3716.

https://doi.org/10.1021/acs.jpcc.1c04005
J. Phys. Chem. C 2021, 125, 20468−20481

(37) Roy, S.; Ramana, C. V. Effect of Thermochemical Synthetic Conditions on the Structure and Dielectric Properties of $Ga_{1.9}Fe_{0.1}O_3$ Compounds. *Inorg. Chem.* **2018**, *57*, 1029−1039.
(38) Zhang, Y.; Yan, J.; Li, Q.; Qu, C.; Zhang, L.; Xie, W. Optical and structural properties of Cu-doped β-Ga_2O_3 films. *Mater. Sci. Eng. B* **2011**, *176*, 846−849.
(39) Chen, C.-C.; Chen, C.-C. Morphology and Electrical Properties of Pure and Ti-Doped Gas-Sensitive Ga_2O_3 Film Prepared by Rheotaxial Growth and Thermal Oxidation. *J. Mater. Res.* **2004**, *19*, 1105−1117.
(40) Oleksak, R. P.; Stickle, W. F.; Herman, G. S. Aqueous-based synthesis of gallium tungsten oxide thin film dielectrics. *J. Mater. Chem. C* **2015**, *3*, 3114−3120.
(41) Zhang, H.; Deng, J.; Duan, P.; Li, R.; Pan, Z.; Bai, Z.; Kong, L.; Wang, J. Effect of Au nanoparticles on the optical and electrical properties of Nb-doped β-Ga_2O_3 film. *Vacuum* **2018**, 465.
(42) Das, S.; Jayaraman, V. SnO_2: A comprehensive review on structures and gas sensors. *Prog. Mater. Sci.* **2014**, *66*, 112−255.
(43) Archer, P. I.; Radovanovic, P. V.; Heald, S. M.; Gamelin, D. R. Low-Temperature Activation and Deactivation of High-Curie-Temperature Ferromagnetism in a New Diluted Magnetic Semiconductor: Ni^{2+}-Doped SnO_2. *J. Am. Chem. Soc.* **2005**, *127*, 14479−14487.
(44) Xu, X.; Zhuang, J.; Wang, X. Synthesis, Self-Assembled 2D Architectures, and Gas-Sensing Properties. *J. Am. Chem. Soc.* **2008**, *130*, 12527−12535.
(45) Kim, H. W.; Na, H. G.; Kwon, Y. J.; Kang, S. Y.; Choi, M. S.; Bang, J. H.; Wu, P.; Kim, S. S. Microwave-Assisted Synthesis of Graphene−SnO2 Nanocomposites and Their Applications in Gas Sensors. *ACS Appl. Mater. Interfaces* **2017**, *9*, 31667−31682.
(46) Chen, M.; Zhang, C.; Li, L.; Liu, Y.; Li, X.; Xu, X.; Xia, F.; Wang, W.; Gao, J. Sn Powder as Reducing Agents and SnO_2 Precursors for the Synthesis of SnO_2-Reduced Graphene Oxide Hybrid Nanoparticles. *ACS Appl. Mater. Interfaces* **2013**, *5*, 13333−13339.
(47) Aguir, K.; Bernardini, S.; Lawson, B.; Fiorido, T. Trends in metal oxide thin films: Synthesis and applications of tin oxide. In *Tin Oxide Materials*; Orlandi, M. O., Ed. Elsevier, 2020, 219−246.
(48) Savioli, J.; Gavin, A. L.; Lucid, A. K.; Watson, G. W. The structure and electronic structure of tin oxides. In *Tin Oxide Materials*; Orlandi, M. O., Ed. Elsevier, 2020, 11−39.
(49) Batzill, M.; Diebold, U. The surface and materials science of tin oxide. *Prog. Surf. Sci.* **2005**, *79*, 47−154.
(50) Ohira, S.; Suzuki, N.; Arai, N.; Tanaka, M.; Sugawara, T.; Nakajima, K.; Shishido, T. Characterization of transparent and conducting Sn-doped β-Ga_2O_3 single crystal after annealing. *Thin Solid Films* **2008**, *516*, 5763−5767.
(51) Kawaharamura, T.; Dang, G. T.; Furuta, M. Successful Growth of Conductive Highly Crystalline Sn-Doped α-Ga_2O_3 Thin Films by Fine-Channel Mist Chemical Vapor Deposition. *Jpn J. Appl. Phys.* **2012**, *51*, No. 040207.
(52) Hao, S. J.; Hetzl, M.; Schuster, F.; Danielewicz, K.; Bergmaier, A.; Dollinger, G.; Sai, Q. L.; Xia, C. T.; Hoffmann, T.; Wiesinger, M.; Matich, S.; Aigner, W.; Stutzmann, M. Growth and characterization of β-Ga_2O_3 thin films on different substrates. *J. Appl. Phys.* **2019**, *125*, 105701.
(53) Dang, G. T.; Kawaharamura, T.; Furuta, M.; Allen, M. W. Mist-CVD Grown Sn-Doped α-Ga_2O_3 MESFETs. *IEEE Trans. Electron Devices* **2015**, *62*, 3640−3644.
(54) Zhao, J. L.; Sun, X. W.; Ryu, H.; Tan, S. T. UV and Visible Electroluminescence From a Sn: Ga_2O_3/n^+-Si Heterojunction by Metal−Organic Chemical Vapor Deposition. *IEEE Trans. Electron Devices* **2011**, *58*, 1447−1451.
(55) Knight, S.; Mock, A.; Korlacki, R.; Darakchieva, V.; Monemar, B.; Kumagai, Y.; Goto, K.; Higashiwaki, M.; Schubert, M. Electron effective mass in Sn-doped monoclinic single crystal β-gallium oxide determined by mid-infrared optical Hall effect. *Appl. Phys. Lett.* **2018**, *112*, No. 012103.
(56) Orita, M.; Ohta, H.; Hirano, M.; Hosono, H. Deep-ultraviolet transparent conductive β-Ga_2O_3 thin films. *Appl. Phys. Lett.* **2000**, *77*, 4166−4168.
(57) Guo, D.; Su, Y.; Shi, H.; Li, P.; Zhao, N.; Ye, J.; Wang, S.; Liu, A.; Chen, Z.; Li, C.; Tang, W. Self-powered ultraviolet photodetector with superhigh photoresponsivity (3.05 A/W) based on the GaN/Sn: Ga_2O_3 p-n junction. *ACS Nano* **2018**, *12*, 12827−12835.
(58) Zhang, J.; Xia, C.; Deng, Q.; Xu, W.; Shi, H.; Wu, F.; Xu, J. Growth and characterization of new transparent conductive oxides single crystals β-Ga_2O_3:Sn. *J. Phys. Chem. Solid* **2006**, *67*, 1656−1659.
(59) Ryou, H.; Yoo, T. H.; Yoon, Y.; Lee, I. G.; Shin, M.; Cho, J.; Cho, B. J.; Hwang, W. S. Hydrothermal synthesis and photocatalytic property of Sn-doped β-Ga_2O_3 nanostructure. *ECS J. Solid State Technol.* **2020**, *9*, No. 045009.
(60) Acosta, Y.; Zhang, Q.; Rahaman, A.; Ouellet, H.; Xiao, C.; Sun, J.; Li, C. Imaging cytosolic translocation of Mycobacteria with two-photon fluorescence resonance energy transfer microscopy. *Biomed. Opt. Express* **2014**, *5*, 3990−4001.
(61) Aguilar, A. C.; Diaz-Moreno, C. A.; Price, A. D.; Goutam, R. K.; Botez, C. E.; Lin, Y.; Wicker, R. B.; Li, C. Non-destructive optical second harmonic generation imaging of 3D printed aluminum nitride ceramics. *Cer. Inter.* **2019**, *45*, 18871−18875.
(62) Price, A. D.; Aguilar, A. C.; Botez, C. E.; Li, C. Optical second harmonic generation imaging and x-ray diffraction of $Cs_{1-x}Rb_xH_2PO_4$ proton conductor series. *J. Appl. Phys.* **2020**, *127*, 193105.
(63) Kohn, J. A.; Katz, G.; Broder, J. D. Characterization of β-Ga_2O_3 and its Alumina Isomorph, θ-Al_2O_3. *Am. Mineral.* **1957**, *42*, 398−407.
(64) Ahman, J.; Svensson, G.; Albertsson, J. A Reinvestigation of β-Ga_2O_3. *Acta Crysta. Sec. C* **1996**, *52*, 1336−1338.
(65) Wang, C. C.; Lee, B. C.; Shieu, F. S.; Shih, H. C. Characterization and photoluminescence of Sn-doped β-Ga_2O_3 nanowires formed by thermal evaporation. *Chem. Phys. Lett.* **2020**, *753*, No. 137624.
(66) Pennington, A. M.; Okonmah, A. I.; Munoz, D. T.; Tsilomelekis, G.; Celik, F. E. Changes in polymorph composition in $P_{25}TiO_2$ during pretreatment analyzed by differential diffuse reflectance spectral analysis. *J. Phys. Chem. C* **2018**, *122*, 5093−5104.
(67) Ghadiri, E.; Shin, D.; Shafiee, A.; Warren, W. S.; Mitzi, D. B. Grain-resolved ultrafast photophysics in $Cu_2BaSnS_{4-x}Se_x$ semiconductors using pump−probe diffuse reflectance spectroscopy and microscopy. *ACS Appl. Mater. Interfaces* **2018**, *10*, 39615−39623.
(68) Kubelka, P. New Contributions to the Optics of Intensely Light Scattering Materials. *J. Opt. Soc. Am.* **1948**, *38*, 448−457.
(69) Siah, S.; Brandt, R.; Lim, K.; Schelhas, L.; Jaramillo, R.; Heinemann, M.; Chua, D.; Wright, J.; Perkins, J. D.; Segre, C. Dopant activation in Sn-doped Ga_2O_3 investigated by X-ray absorption spectroscopy. *Appl. Phys. Lett.* **2015**, *107*, 252103.
(70) Epperlein, D.; Dick, B.; Marowsky, G.; Reider, G. A. Second-harmonic generation in centro-symmetric media. *Appl. Phys. B: Lasers Opt.* **1987**, *44*, 5−10.
(71) Ashwell, G. J.; Jefferies, G.; Hamilton, D. G.; Lynch, D. E.; Roberts, M. P. S.; Bahra, G. S.; Brown, C. R. Strong second-harmonic generation from centrosymmetric dyes. *Nature* **1995**, *375*, 385−388.
(72) Timofeeva, M.; Bouravleuv, A.; Cirlin, G.; Shtrom, I.; Soshnikov, I.; Reig Escalé, M.; Sergeyev, A.; Grange, R. Polar second-harmonic imaging to resolve pure and mixed crystal phases along GaAs nanowires. *Nano Lett.* **2016**, *16*, 6290−6297.
(73) Zhu, Y.; Lin, Q.; Zhong, Y.; Tahini, H. A.; Shao, Z.; Wang, H. Metal oxide-based materials as an emerging family of hydrogen evolution electrocatalysts. *Energy Environ. Sci.* **2020**, *13*, 3361−3392.
(74) Sun, X.; Li, K.; Yin, C.; Wang, Y.; He, F.; Bai, X.; Tang, H.; Wu, Z. The oxygen reduction reaction mechanism on Sn doped graphene as an electrocatalyst in fuel cells: a DFT study. *RSC Adv.* **2017**, *7*, 729−734.
(75) Yu, J.; Ma, F. X.; Du, Y.; Wang, P. P.; Xu, C. Y.; Zhen, L. In Situ Growth of Sn-Doped Ni_3S_2 Nanosheets on Ni Foam as High-Performance Electrocatalyst for Hydrogen Evolution Reaction. *ChemElectroChem* **2017**, *4*, 594−600.

https://doi.org/10.1021/acs.jpcc.1c04005
J. Phys. Chem. C 2021, 125, 20468−20481